Ceria-Co-Cu-based SOFC anode for direct utilisation of methane or ethanol as fuels

Sarruf, Bernardo; Hong, Jong-Eun; Steinberger-Wilckens, Robert; Miranda, Paulo Emilio

DOI:
10.1016/j.ijhydene.2019.04.075

Document Version
Peer reviewed version

Citation for published version (Harvard):
Sarruf, B, Hong, J-E, Steinberger-Wilckens, R & Miranda, PE 2019, 'Ceria-Co-Cu-based SOFC anode for direct utilisation of methane or ethanol as fuels', *International Journal of Hydrogen Energy*.
https://doi.org/10.1016/j.ijhydene.2019.04.075

to be published in IJHE WHEC 2018 special issue in 2019

Ceria-Co-Cu-based SOFC anode for direct utilisation of methane or ethanol as fuels

Bernardo Jordão Moreira Sarruf[ab*], Jong-Eun Hong[c],
Robert Steinberger-Wilckens[b], Paulo Emílio Valadão de Miranda[a]

[a]*Hydrogen Laboratory COPPE, Metallurgical and Materials Engineering, Federal University of Rio de Janeiro - 21942-971 Rio de Janeiro, RJ, Brazil*
[b]*Centre for Fuel Cell and Hydrogen Research - School of Chemical Engineering, University of Birmingham, Edgbaston, Birmingham, B15 2TT, UK*
[c]*Fuel Cell Laboratory - Korea Institute of Energy Research, 152, Gajeong-ro, Yuseong-gu, Daejeon 34129, South Korea*

Abstract

Nickel-free solid oxide fuel cell anodes are an object of study for applications that aim at utilising primary carbonaceous fuels to generate power. In this study, a ceria-Co-Cu anode is produced and tested with hydrogen, methane and ethanol fuels at various temperatures.

The produced catalysts were characterised by X-ray analysis and H_2 temperature-programmed reduction (TPR). Catalytic tests were performed and compared with the material under electrochemical operation. The cells were electrochemically characterised by recording i-V plots. The samples were assessed post-test for eventual carbon deposits by Raman spectroscopy investigations and temperature-programmed oxidation (TPO) analysis.

The cells were able to operate with hydrogen, methane as well as ethanol, directly fed to the anode, with maximum power densities ranging from 400 to 540 $mW.cm^{-2}$, depending on the fuel stream utilised. The cells also kept their integrity demonstrating coking resistance for over 24 hours of continuous operation. Important discussions and conclusions are drawn about carbon formation and the role of each compound in the anode composition. The bimetallic cell (ceria-Co-Cu) is herein compared to monometallic ones (ceria-Co and ceria-Cu) that served as baselines. The advantages of the bimetallic composition are listed and evaluated throughout the discussions.

***Keywords**:* Solid oxide fuel cells, nickel-free anode, direct methane, ethanol utilisation, primary fuels

*Corresponding author **Email address: sarruf@labh2.coppe.ufrj.br (Bernardo Sarruf)**

1. Introduction

Solid oxide fuel cells - SOFCs - are one of the main promises for high-efficiency stationary and mobile power generation technologies. This is due especially to their fuel flexibility and modularity characteristics, fitting them to a wide range of applications.

The development of micro units of combined heat and power - μ-CHPs - for domestic applications have been gaining space, consolidating the SOFC technologies as an important part of a more sustainable energy economy. However, one of the main obstacles for concepts deployment and market introduction is the transition in infrastructure needed for a complete hydrogen economy so that the end consumer can fully enjoy the currently ready-to-market technologies. The distribution and cost of hydrogen is still an important issue raised when the operational expenditures (OPEX) of running such systems is calculated. From this issue, is born the most important advantage of high temperature fuel cells: their fuel flexibility.

The possibility of feeding primary fuels such as biogas, methane- or hydrogen-rich fuels, liquid ethanol, amongst others, directly into an SOFC stack producing electricity and heat with high efficiency - as depicted in Figure 1 - is one of the short-term mitigating actions for cost reduction that are well scrutinised in the literature [1-4].

Carbon deposition on the anode is a serious concern in the case of unreformed hydrocarbons or alcohols as fuels in conventional nickel-based SOFCs. As is well-known, carbon adheres strongly to nickel surfaces, deactivating them and destroying the anode microstructure [5-8]. A balance has to be found between carbon adhering to the nickel catalyst in the conversion process and its removal by oxidative processes.

Some works have been done in alloying nickel particles aiming to hinder coking activity. Is reported that the insertion of silver [9, 10], tin [11], copper [12], gold and molybdenum [13, 14, 15] metallic particles enhance the resistance of the nickel-based anode towards carbon deposition. The metallic alloying over nickel, promotes partial passivation, decreasing the high coking activity that associated with metallic.

Additionally, perovskite- and double-perovskite-based anode has been evaluated for direct hydrocarbon utilisation. In addition to lower coking activities, these structures have the advantage of being highly mechanical resistant under redox cycling. Therefore, eventual carbon deposition can be easily removed by flushing oxygen-rich gas into the anode to oxidise carbon [16-18]. Another solution for this matter is the development of new nickel-free materials that can guarantee even lower activity for coking [19-21].

The primary fuel direct utilisation or electrochemical oxidation is a reaction path that avoids carbon formation. Under anhydrous conditions, since there is no oxidising agent, such as steam or carbon oxides, cracking is most likely to occur, since it requires lower energies, as depicted in Equation 1.

$$CH_4 \rightarrow C + 2H_2, \qquad \Delta H = +75\ kJ.mol^{-1} \qquad (1)$$

However, under a considerable source of oxygen ions it is less energetic to promote partial electrochemical oxidation of methane, for instance, as per Equation 2.

$$CH_4 + O^{2-} \rightarrow CO + 2H_2 + 2e^-, \qquad \Delta H = -36\ kJ.mol^{-1} \qquad (2)$$

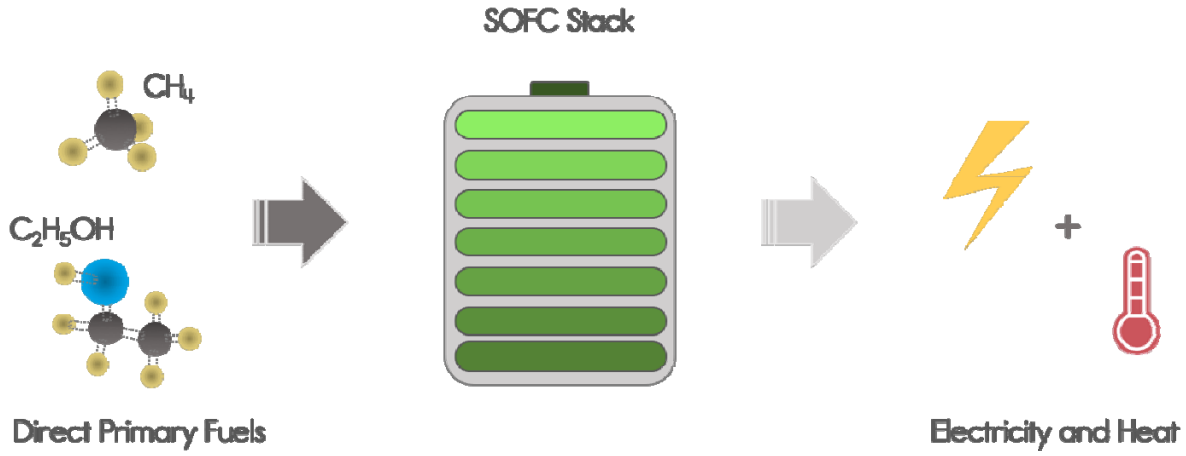

Figure 1. Power co-generation with direct primary fuels.

Hence, for the SOFC case, there are two conditions to be considered: the thermodynamic conditions, which the reactants are submitted to, when open circuit voltage governs; and the electrocatalytic conditions that prevail when the circuit is closed.

This study looks into enabling the operation of SOFC with ethanol by developing a cobalt-rich catalyst, with ceria as the selected material to give mixed-ionic-electronic characteristics to the composition, and copper to enhance electrical properties as well as carbon post oxidation ability. Furthermore, tests were designed targeted at determining the main differences between the operation under electrical load and mere catalytic conditions. Baseline catalyst compositions were produced so that the role of each metal in the present work could be further understood.

2. Experimental

2.1 Electrocatalyst Production and Characterisation

The experiments were designed to test the specific role of each of the metals in the anode composition in handling carbon oxidation. Therefore, ceria-based electrocatalysts were produced as two monometallic compositions as baselines (CeO_2-Co and CeO_2-Cu) and a bimetallic composition (CeO_2-Co-Cu), which was the very aim of this work.

All three compositions were produced by the amorphous citrate method. This synthesis route consists in dissolving the desired molar proportion of the precursor salts individually in deionised water up to the solubility limit. An aqueous solution of citric acid was added to each salt solution, also individually, targeting at having 1 mol of citric acid to 1 mol of cation of each salt. After that, the solutions were mixed and kept under magnetic stirring at 70˚C, whilst the pH values were slowly neutralised with ammonium hydroxide. The solutions were then dried until a gel was formed, which was dried at 90˚C and finally combusted to ashes at 200˚C for 6 hours. The ashes were finally pulverised in an agate mortar and heat treated at 800˚C for 2 hours. The three powder compositions produced were in a molar proportion of Ce:Co:Cu = 1:1:0, 1:0:1 and 1:2:1.

X-ray diffraction patterns were taken for the three compositions using a Bruker D8 diffractometer, ranging from 10 to 90˚, in steps of 0.02˚. The X-ray radiation source was Cu$K\alpha$ = 0.15418 nm with an acceleration voltage of 40 kV and 30 mA electric current.

H_2-Temperature-programmed reduction – TPR – was performed over the bimetallic powder to determine the reducibility of the catalyst. TPR analysis was carried out using a Quantachrome ChemBET Pulsar TPR/TPD equipment that ranged from room temperature to 900˚C, in steps of 5 ˚C.min^{-1} over approximately 20 mg of powder in a quartz reactor. The gas mixture consisted of 5% H_2, balanced by N_2.

The bimetallic powder was submitted to treatment with anhydrous methane at 800˚C, followed by Raman spectroscopy of the sample's surface, prior to oxidation, to observe carbon deposits under thermodynamic equilibrium catalytic conditions. Raman spectroscopy was taken over the powder post-treatment with a 633 nm wavelength laser in a Renishaw in Via Raman microscope. The sample was scanned at several spots from 100 to 3200 cm^{-1} within 20 seconds acquisition time and 1% of the laser total power.

After this test, the powder was also submitted to a catalytic test with methane to determine its behaviour under a carbonaceous fuel flow and in-situ catalytic conditions. For that, an aliquot of powder (around 100 mg) was placed in a quartz tube, sandwiched by quartz wool and placed in a furnace. The temperature was raised up to 500˚C under nitrogen atmosphere, then from 500 to 800˚C the atmosphere was switched to a reducing gas mixture (40% vol. hydrogen in balanced nitrogen). The outlet gas was coupled to a gas chromatograph (Shimadzu GC-2014) in which organics such as methane were quantified by a flame ionisation detector (FID) and inorganics such as carbon oxides could be determined by a thermal conductivity detector (TCD). After a few minutes in hydrogen at 800˚C, a couple of products injections were performed to account for any residual carbon oxide that could be found. These residual readings were used as a baseline and were further subtracted from the actual results. Finally, after the conditions were judged as steady, a methane atmosphere (40% vol. anhydrous methane in balanced nitrogen) was flushed into the sample. The injections were done until an outflow of methane was observed constant above 120 × 10^{-7} mol.ml^{-1} and practically no carbon oxide was noticed anymore. To finish the analysis, the reactor was cleaned with a flow of nitrogen (99.999% pure) still at 800˚C and a

flow of synthetic air was opened to oxidise eventual deposits of carbon that were read by the GC as carbon oxides. This procedure was devised to verify the eventual presence of significant amounts of carbon oxides that could confirm the presence or absence of carbon deposition originated from catalytic cracking.

2.2 Cell fabrication, testing and post-mortem characterisation

SOFC button cells for testing the anode compositions were fabricated by screen printing ceramic suspensions over a 150 μm thick electrolyte support from Fuel Cell Materials. Prior to cell assembly, attention was given to the thermal mismatch between the electrolyte material (scandia and ceria stabilised zirconia, 10Sc1CeSZ) and the metallic compounds of the anode (cobalt and copper). Whilst the electrolyte has coefficients of thermal expansion of 13-14 × 10^{-6}, copper and cobalt oxides range from 5 to 7 × 10^{-6}. The situation worsens when these oxides are reduced to metals, having their CTEs increased to around 17 × 10^{-6} [22-25]. For that matter, a porous buffer layer was developed to hinder the effects of anode/electrolyte delamination during heating and oxides' reducing procedures. The buffer porous layer consisted of a mixture of electrolyte material and pure ceria. An ink suspension of this material was deposited by screen printing over the 10Sc1CeSZ electrolyte support and sintered in air at 1300˚C for 3 hours, as depicted in Figure 2. The strontium-doped lanthanum manganite – LSM – cathode was deposited onto the other surface of this electrolyte and sintered at 1100˚C for 2 hours. Finally, CeO_2-Co, CeO_2-Cu, CeO_2-Co-Cu, anodes were deposited over the buffer layer and dried at 800˚C for 2 hours, as shown in Figure 2. The production delivered 3 cells: two monometallic baseline cells (CeO_2-Co and CeO_2-Cu) and one bimetallic cell (CeO_2-Co-Cu). After single cell production, silver wires aided by silver paste were connected to the electrodes to serve as current collectors. The electrodes were designed to be over 30 μm of thick.

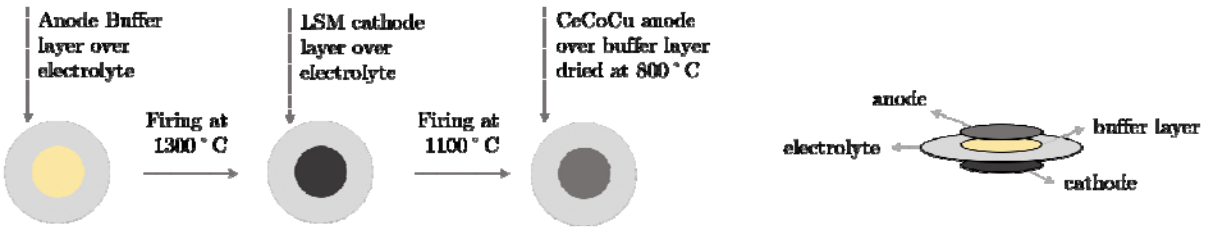

Figure 2. Cell fabrication, step-by-step scheme.

The electrochemical tests consisted of i-V plots recording as temperatures ranging from 750 to 850˚C for the monometallic cells in hydrogen, from 700 to 800˚C for the bimetallic cell in hydrogen. All cells were tested under anhydrous methane and then anhydrous ethanol at 850˚C. The operation

temperatures for the tests in hydrogen were shifted since the bimetallic cells have shown evident higher performance, thus dismissing the necessity of raising the temperature above 800˚C in this case.

After operation under carbonaceous fuel conditions for at least 24 hours, Raman spectroscopy was performed over the anode surfaces with the same conditions detailed in the previous section. Temperature-programmed oxidation was conducted over the bimetallic cell to confirm the absence of carbon deposits. Similarly, to the oxidation tests described for the electrocatalyst powder, the temperature at the anode surface was raised from room temperature to 850˚C whilst a flow of 5% vol. oxygen in balanced nitrogen served as oxidiser. The outlet products were quantified by gas chromatography.

Anodes of all three compositions were fabricated to be submitted to ageing treatment in hydrogen at 800˚C. The half cells were kept in tubular furnace with hydrogen flow for 1 hour and then for 100 hours. The cross-section of each cell was thus evaluated by scanning electron microscopy so the differences between monometallic and bimetallic cells could be compared. Energy-dispersive X-ray spectroscopy was used to observe phase distribution along the anode bulk.

3. Results and discussion

X-ray diffraction (XRD) patterns are shown in Figure 3 for the three anode compositions synthesised. The sharp and narrow peaks identify the phases ceria, cobalt oxide, and copper oxide. The ceria phase appears as the cubic fluorite phase, compatible with the zirconia-based buffer layer and electrolyte materials. The formation of solid solution between ceria and the anode metals are less likely to occur due to the partial reduction of ceria in reducing atmospheres. The details of the Rietveld refinement with lattice calculations as well as expected composition were previously published by the authors [19]. The spinel phase of the cobalt oxide as well as the tenorite phase for the copper oxide, have low solubility in the ceria lattice as per their respective phase diagrams found in [26-29].

The H_2-temperature-programmed reduction (TPR) profile is shown in Figure 4 for the bimetallic powder composition. The TPR profile shows 6 well-defined peaks highlighted after Gaussian deconvolution and depicted over the raw data. The first and the fourth peaks at 207 and 279˚C are due cobalt oxide reduction according to Equations 3 and 6, whereas the peaks at 228 and 258˚C represent the consumption of hydrogen for total reduction of copper oxide taking place as shown in Equations 4 and 5, respectively.

$$Co_3O_4 + H_2 \rightarrow 3CoO + H_2O \quad (3)$$

$$2CuO + H_2 \rightarrow Cu_2O + H_2O \quad (4)$$

$$Cu_2O + H_2 \rightarrow 2Cu + H_2O \quad (5)$$

$$CoO + H_2 \rightarrow Co + H_2O \quad (6)$$

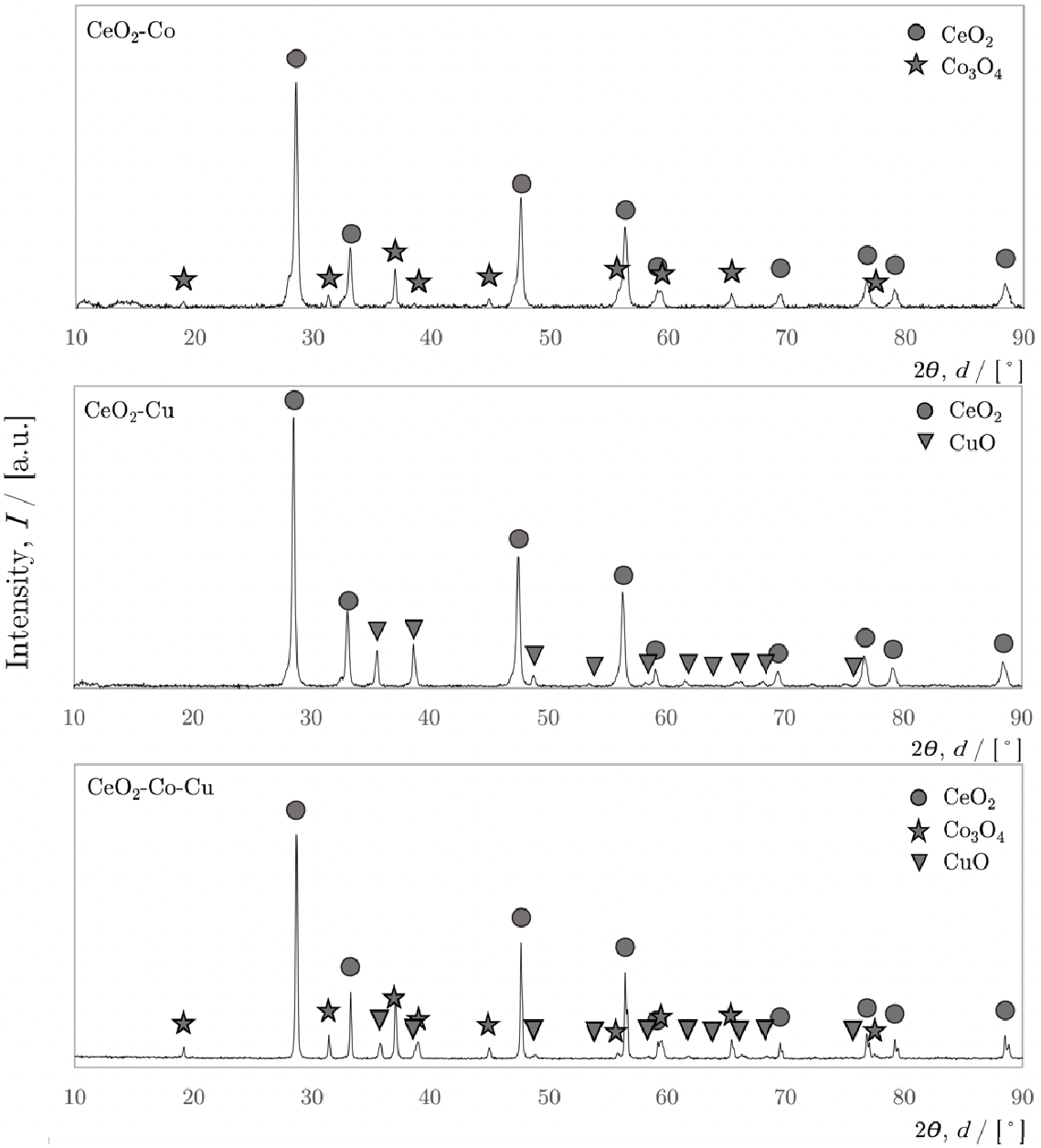

Figure 3. X-ray patterns for compositions CeO_2-Co, CeO_2-Cu, and CeO_2-Co-Cu.

Regarding cerium oxide, the reduction process is defined by the peaks at higher temperatures. The reduction of CeO_2 will occur partially turning Ce^{4+} into Ce^{3+} as represented by Equation 7. Firstly, the surface capping oxygen anions attached to the Ce^{4+} surface with an octahedral coordination will react with hydrogen at temperatures between 500 and 650˚C. Then, finally, oxygen from the ceria bulk structure will be released at temperatures above 750˚C [30, 31].

$$CeO_2 + \delta H_2 \rightarrow CeO_{2-\delta} + \delta H_2O \quad (7)$$

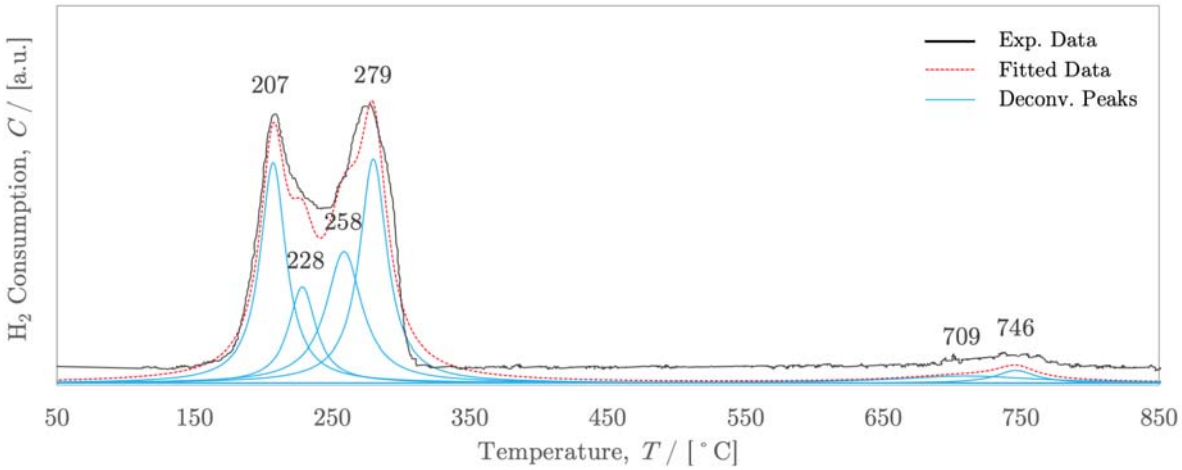

Figure 4. H_2-Temperature-programmed reduction for the CeO_2-Co-Cu electrocatalyst.

Furthermore, the total consumption of hydrogen per gram of catalyst was estimated as 8×10^{-3} mol. Accounting for an oxygen uptake of around half of the hydrogen consumption in mols, thus 4×10^{-3} mol per gram of catalyst, and considering the area of the peaks assigned to the ceria reduction, the oxygen deficiency can be estimated as around 5.5% and thereby the structure of cerium oxide after reduction was $CeO_{1.89}$ as per Equation 7.

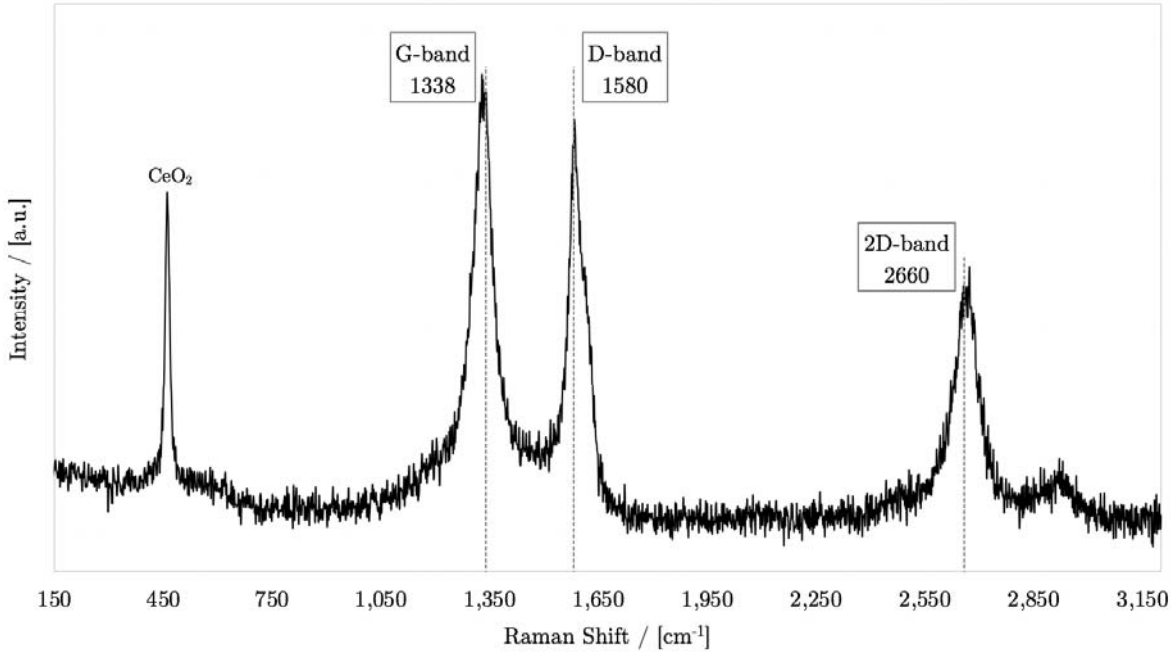

Figure 5: Raman spectrum for the bimetallic powder treated in methane at 800˚C.

After the analysis of the raw powder, the catalyst was treated in methane and the results of hydrocarbon decomposition are shown in the Raman spectrum of Figure 5. The powder was submitted to a flow of pure methane at 800˚C for 2 hours and the most notable result were the peaks assigned to the various bands of carbon at 1338, 1580, and 2660 cm^{-1}. The presence of the ceria peak was also observed at 460 cm^{-1}, and the other oxides or metals were not sensed, probably due to the expressiveness of the carbon peaks. This analysis confirms that the cobalt-rich catalyst powder is prone to carbon deposition

under thermodynamic equilibrium catalytic conditions, when no oxygen or oxygen ions source is involved.

Therefore, the test was redesigned with a gas chromatograph coupled to the outlet flow, for further understanding of the carbon deposition process over the catalyst. In Figure 6, it can be seen that the catalyst reduction/activation from 500 to 800˚C lasts for over an hour to assure full reduction and steady-state condition. At 800˚C after the methane mixture was added, four subsequent products injections shifted by 15 minutes amongst each other, guaranteed that no residual carbon oxide was present and the flow of methane was being fully wasted, rather than cracked. Finally, the air flow oxidised the samples and the presence of carbon dioxide and carbon monoxide was recorded, mainly within the first injection into the gas chromatograph. This second test confirmed that under these catalytic conditions, with the dispersed powder placed in a fixed bed reactor at high temperature with no electrical charge or oxygen ions supplied for electrochemical oxidation, carbon deposition is favoured.

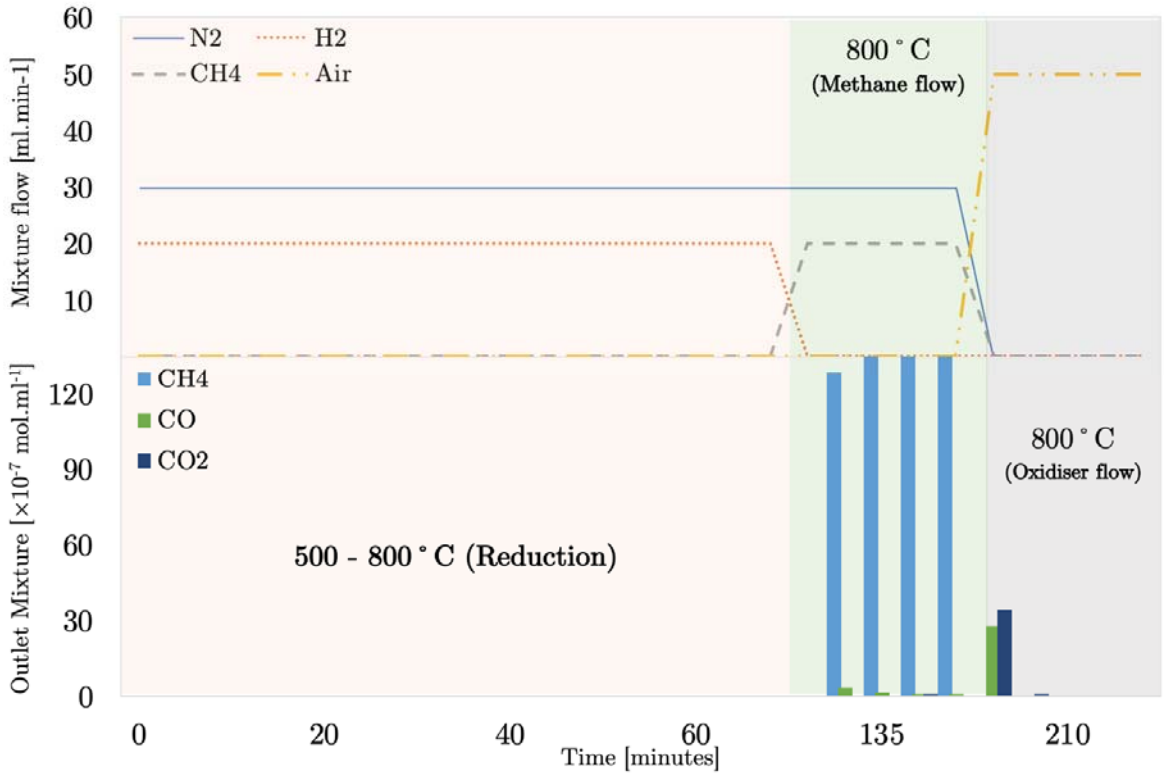

Figure 6: Catalytic tests for the bimetallic powder and carbon oxidation behaviour after methane treatment at 800˚C.

The i-V plots for all electrochemical tests are shown in Figure 7. Figure 7a shows the plots for CeO_2-Co with hydrogen as fuel at 750, 800, and 850˚C. The maximum power densities for these conditions were 104.3, 157.4, and 263.3 $mW.cm^{-2}$, whereas the open circuit voltages – OCV – were 1.12, 1.11, and 1.09 V, respectively from 750 to 850˚C.

Figure 7b shows the results for the CeO_2-Cu cell, showing considerably lower performance, thus highlighting the catalytic role of cobalt. The maximum power densities for this cell in hydrogen were 43.1, 76.6, and 127.2 $mW.cm^{-2}$, with OCVs of 1.15, 1.12, and 1.11 V from 750 to 850˚C, respectively.

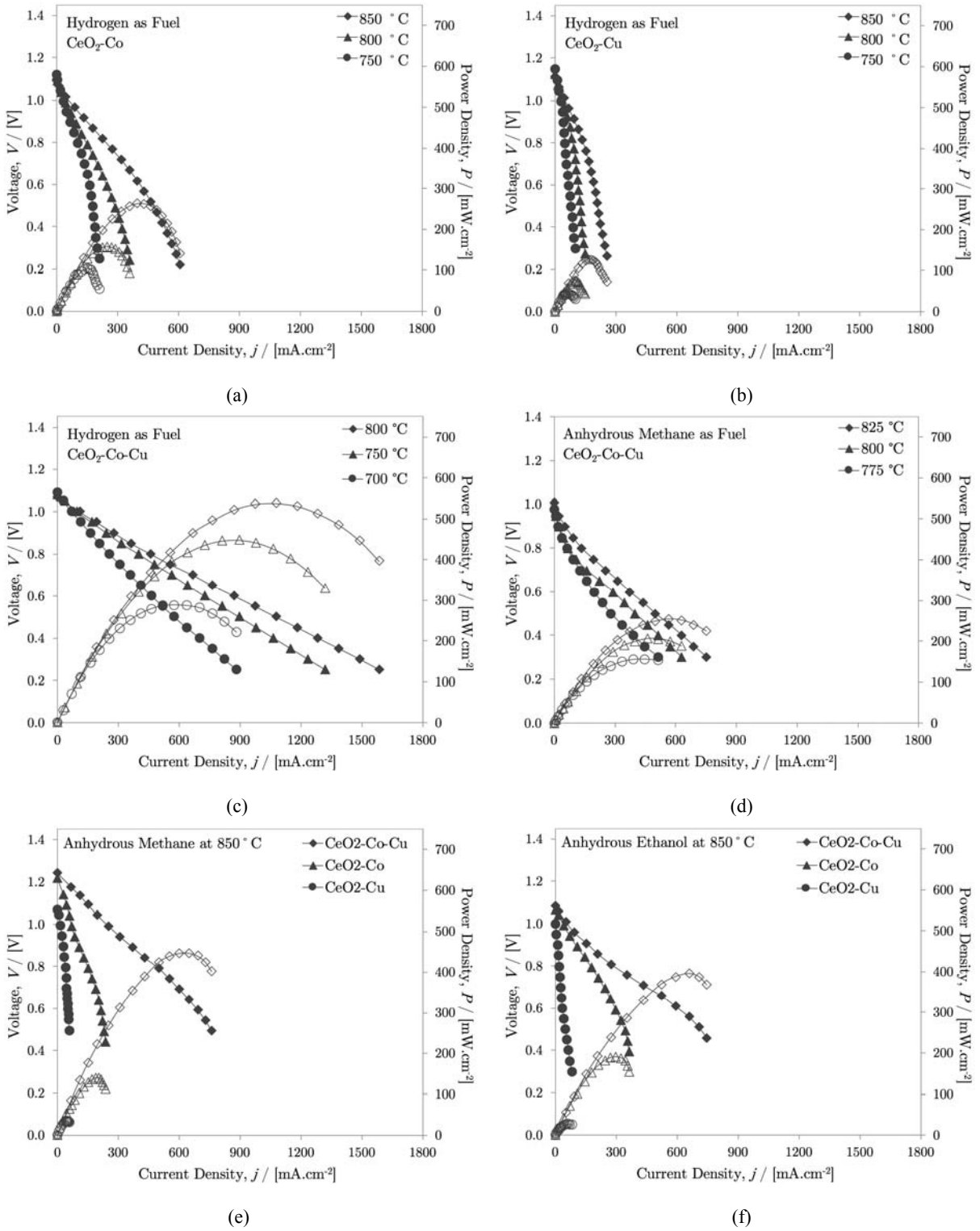

Figure 7: Electrochemical performance tests for (a) CeO_2-Co with hydrogen as fuel, (b) CeO_2-Cu with hydrogen as fuel (c) CeO_2-Co-Cu with hydrogen as fuel, (d) CeO_2-Co-Cu with methane as fuel, (e) all three compositions at 850˚C with methane as fuel, and (f) all three compositions at 850˚C with ethanol as fuel.

Taking into account the results of the monometallic cells as baseline, the performance of the bimetallic cell, shown in Figure 7c, is thus substantially higher even at lower temperatures. The i-V plots with hydrogen as fuel were recorded from 700 to 800˚C presenting maximum power densities of 287.8, 447.4, and 538.1 $mW.cm^{-2}$, whereas OCVs were also adequate, being 1.09, 1.08, and 1.07 V from lower to higher temperature.

After tests with hydrogen confirmed the suitability of the cells, the fuel was then switched to anhydrous methane. Figure 7d presents the performance of the bimetallic cell at various temperatures with methane as fuel, when maximum power densities were 156.6, 206.8, and 254.6 mW.cm^{-2} and OCVs were 0.98, 0.99, and 1.00 V. An inverse behaviour of the open circuit voltage can be observed in this case, which is explained by thermodynamics. In the case of unreformed or even partially reformed methane, to consider the Nernst Equation 8 is a common mistake.

$$E_n = -\frac{\Delta G}{2F} + \frac{RT}{2F}\ln\left(\frac{P_{H_2}\cdot\sqrt{P_{O_2}}}{P_{H_2O}}\right) \quad (8)$$

Instead, locally dependant OCV changes are to be considered, since several different reactions occur simultaneously, such as methane electrochemical oxidation, methane steam reforming (owing to the fact that water is inevitably produced by electrochemical oxidation), as well as water-gas shift reactions etc. In other words, the ratio P_{H2}/P_{H2O} becomes heterogeneous throughout the anode's bulk, and the OCV has to be considered as the local equilibrium potential of all charges between anode and cathode [32-34].

In Figure 7e the bimetallic cell was compared to the baseline monometallic versions when anhydrous methane served as a fuel at higher temperatures, such as 850˚C. Again, the performance of the bimetallic cell was much higher, showing a maximum power density of 446.4 mW.cm^{-2}, whereas CeO_2-Co and CeO_2-Cu delivered 139.9 and 34.2 mW.cm^{-2}, respectively. The OCVs were 1.23, 1.21, and 1.07 V for the CeO_2-Co-Cu, CeO_2-Co, and CeO_2-Cu combinations, respectively.

The higher OCV for the cells with cobalt content can be explained by the decomposition of the fuels over this catalyst. It is important to highlight that the anode under OCV conditions behaves as a catalyst rather than electrocatalyst, and the previous tests showed that under these conditions, methane cracking, hence carbon deposition, occurs. Therefore, under OCV conditions the reactants will be a mixture of hydrogen, and carbonaceous compounds that can be oxidised when current is present, thus electrochemically producing carbon oxides. This mixture of reactants, resulted from electrochemical oxidation, can lower the oxygen concentration even more, which increases the open circuit voltage.

Finally, in Figure 7f the i-V plots for all three compositions at 850˚C, using anhydrous ethanol as fuel is shown. As expected, the result for the bimetallic cell is the highest, 395.4 mW.cm^{-2}, followed by 190.1 and 27.7 mW.cm^{-2}, for the CeO_2-Co and CeO_2-Cu cells, respectively. Cells' OCVs in this case were 1.08, 1.07, and 1.00 V, thus following the trend of a hydrogen-rich fuel. All results of maximum power densities at all various conditions are summarised in Table 1 for comparison.

Results from Ce-Co-Cu cells are reported by [35] as being around 260 mW.cm^{-2} with methane as fuel at 800˚C. Lee *et al.* [36] report having achieved around 350 mW.cm^{-2} within their Ce-Co-Cu cells fuelled with n-butane as fuel at 800˚C. Ni-Cu cells were also tested in the literature [36] delivering 150 mW.cm^{-2} with n-butane at 700˚C. Results with ethanol as fuel in Nickel-alloyed tin are reported as 200-

250 mW.cm^{-2} [9] and 320 mW.cm^{-2} [11] with biogas. Gavrielatos *et al.* [10] report 100 mW.cm^{-2} of power density for their Nickel-Ag cell under methane steam reforming conditions at 700˚C.

Table 1: Maximum power densities for all temperature and fuel conditions.

Anode Composition	Fuel	Temperatures					
		700˚C	750˚C	775˚C	800˚C	825˚C	850˚C
CeO_2-Cu	Hydrogen	----	43.1	----	76.6	----	127.2
	Methane	----	----	----	----	----	34.2
	Ethanol	----	----	----	----	----	27.7
CeO_2-Co	Hydrogen	----	104.3		157.4		263.3
	Methane	----	----	----	----	----	140.0
	Ethanol	----	----	----	----	----	190.1
CeO_2-Co-Cu	Hydrogen	287.8	447.4	----	538.1	----	----
	Methane	----	----	156.6	206.8	254.6	446.4
	Ethanol	----	----	----	----	----	395.4

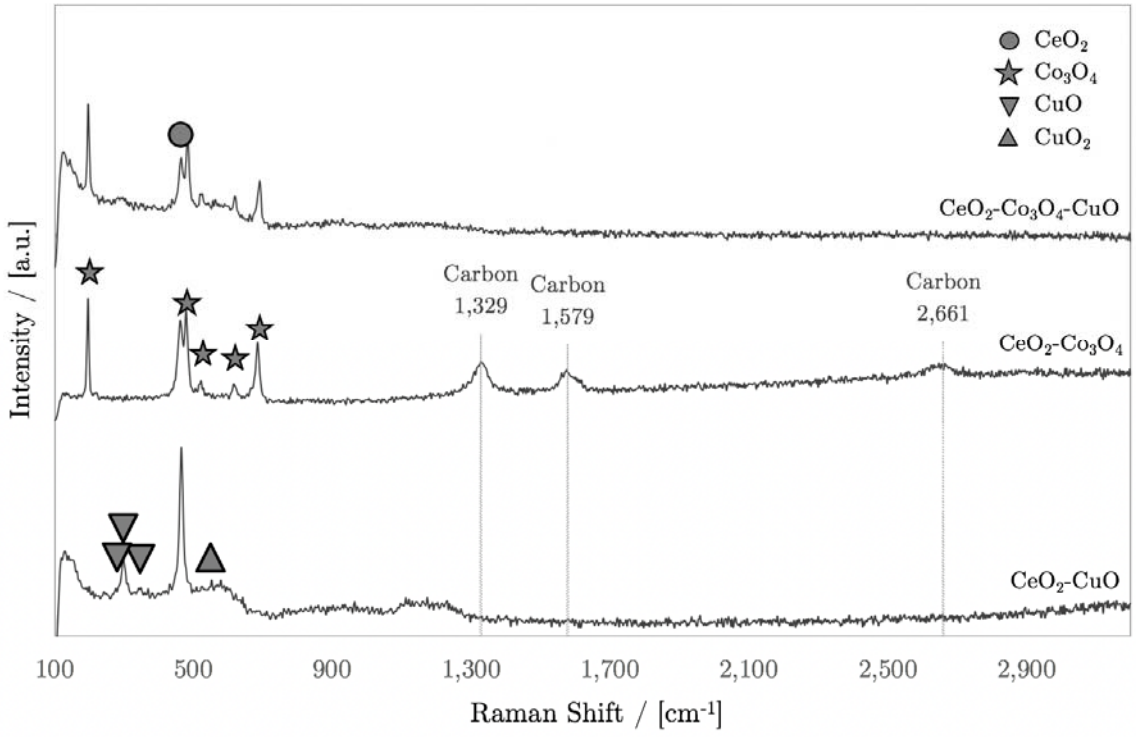

Figure 8: Raman spectra for compositions Ce-Co-Cu, Ce-Co and Ce-Cu.

After testing the cells, Raman spectroscopy scans were performed over the operated anode surfaces. In Figure 8 the peaks of ceria at 460 cm^{-1} [37], cobalt oxides at 196, 482, 523, 621 and 691 cm^{-1} [38, 39], CuO at 158, 286 and 347 cm^{-1}, as well as Cu_2O at 550 cm^{-1} [40] are highlighted. The most important result from these spectra is the confirmation of the absence of carbon over the surface of the bimetallic cell. Furthermore, it is also notable that whilst the CeO_2-Co anode showed to be prone to coke formation,

the CeO_2-Cu showed no evidence of carbon deposits, confirming the important role of copper on preventing coking.

The Raman analysis clearly defined the importance of each metal in the electrocatalyst composition. It is confirmed that the bimetallic electrocatalyst withstands coking under electrochemical conditions, whereas the monometallic CeO_2-Co anode shows to be highly catalytically active for methane cracking and carbon deposition due the absence of copper. In the case of the bimetallic anode, copper is known to facilitate carbon post-oxidation prior to anode depletion [35, 36], which means that it prevents anode coking.

The investigations on carbon deposition were led further by performing temperature programmed oxidation over the operated anode. Therefore, any residual carbon deposited in the anode's bulk would be post-oxidised into carbon oxide and traced by the GC. Figure 9 shows, in comparison, two TPO profiles: the first is a baseline with a known aliquot of graphite powder and the second is the post-operated cell. The baseline test shows a typical carbon oxidation profile with increasing temperature, presenting carbon monoxide formation at lower temperatures, such as 300-500˚C and carbon dioxide at higher temperatures. Comparing the baseline test, that was run with a 5 mg aliquot of graphite, the amount of residual carbon deposited in the anode was estimated as being a few milligrams, or less than 5% wt. of the total anode mass.

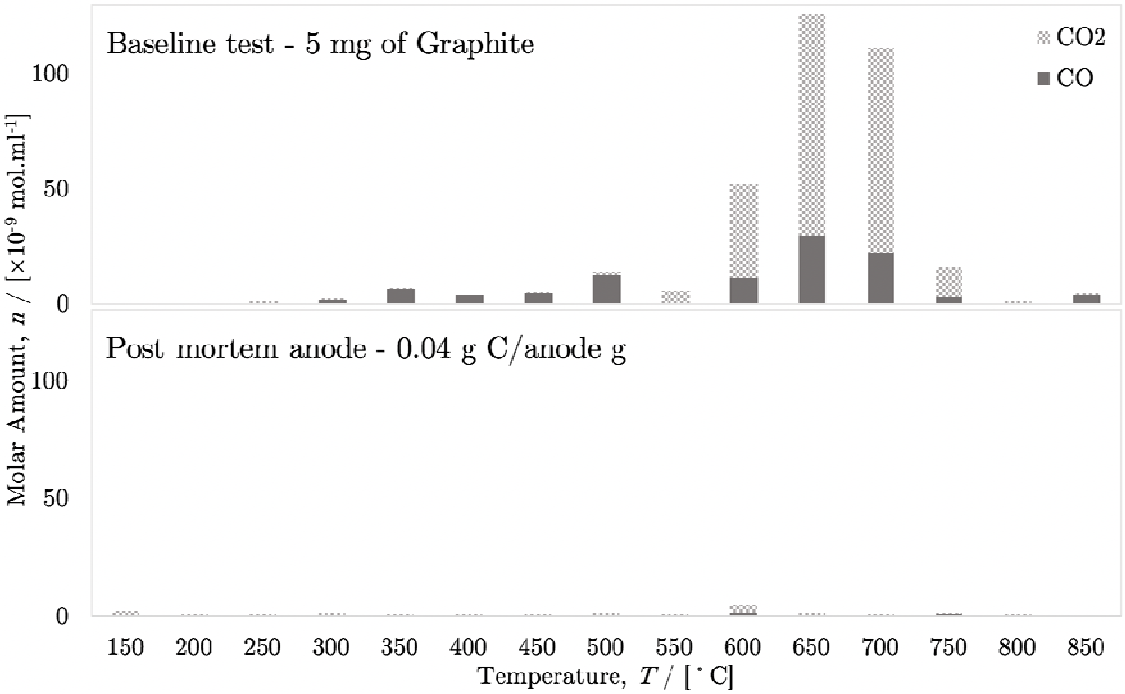

Figure 9: Temperature-programmed oxidation for Graphite powder and the CeO_2-Co-Cu anode after operation with carbonaceous fuels.

Therefore, since the anode's density was around twice as high as that of graphite, the volumetric fraction of carbon deposits was less than 10%. It is important to highlight that the maximum amount of carbon oxide measured by the CG in this case, was 3.2×10^{-9} mol of CO_2, which was so insignificant that it could be accounted as residual. In Figure 6, it was discussed that, whilst the amount of methane being flushed was constant, the amounts of carbon oxides were residuals and in the order of 13×10^{-9} mol of

CO_2. When the carbon oxidation occurred in the catalytic analysis depicted in Figure 6, the amounts of carbon oxides were in the order of 3×10^{-6} mol of CO_2, and thus 3 orders of magnitude higher than in the electrocatalytic case.

The cross sections of the half cells are shown in Figure 10. The left-hand images show each anode after a reducing treatment at 800˚C for 1 hour, whereas the right-hand images show the same anode after 100 hours at the same aforementioned conditions. The circled images show the energy dispersive X-ray spectroscopy (EDS) results for phase distribution. EDS images were used to determine elements position, and the elements are represented as yellow (ceria), red (cobalt) and blue (copper). The layers of the anode were originally designed to be around 10-12 μm thick – regarding the buffer layer – and 20-25 μm thick regarding the catalytic layer.

The first notable results from Figures 10a and 10b are both the difficulty of visually identifying the different layers, and the reduced thickness of these ensembled layers. In Figure 10a it can be spotted that the cobalt content of the anode, is presented mainly over the surface, suggesting evaporation. In Figure 10b, the copper content is better dispersed, after 100 hours. However, copper particles are intensively coarser even after the 1-hour treatment. As a consequence of coarsening, it is observed that the decrease in porosity levels is evident for microstructures of Figures 10a and 10b.

The bimetallic anode, which shows its microstructure in Figure 10c, shows the integrity of the two original anode layers. In both cases (1 hour and 100 hours) treatment, the layer thicknesses remain the same. Additionally, phase distribution is homogeneous, showing a ceria-rich content in the first layer and a bimetallic well-kept particle distribution in the second layer.

One of the major issues with copper-added anodes is sintering and coarsening due copper's low melting point. When a bimetallic composition is concerned, as long as the metallic particles are well dispersed, there will be lesser contact between copper-copper and cobalt-cobalt particles, which delays self-diffusion. The self-diffusive coefficients of cobalt and copper at 800˚C are 2.02×10^{-8} [41] and 2.37×10^{-7} $m^2.s^{-1}$ [42], respectively, whereas inter-diffusive coefficient amongst copper and cobalt is around 10^{-16} $m^2.s^{-1}$ [43]. Therefore, the bimetallic dispersion serves as a barrier against self-diffusion, preventing agglomeration, and coarsening of particles.

Furthermore, it is expected around 25-27% vol. of metallic phase for the monometallic anodes herein presented, whereas for the bimetallic one 32% vol. of cobalt and 18% vol. of copper is the order of magnitude. Therefore, the metallic load in the bimetallic anode is expected to be twice higher than those of the monometallic ones. The higher metallic load will also provided higher electrical conductivity, which explains the higher performance in this case. However, in addition to that, all other facts such as: increased thermal stability, decreased carbon deposition and ability to keep a homogenous microstructure over time, contributed to a better performance.

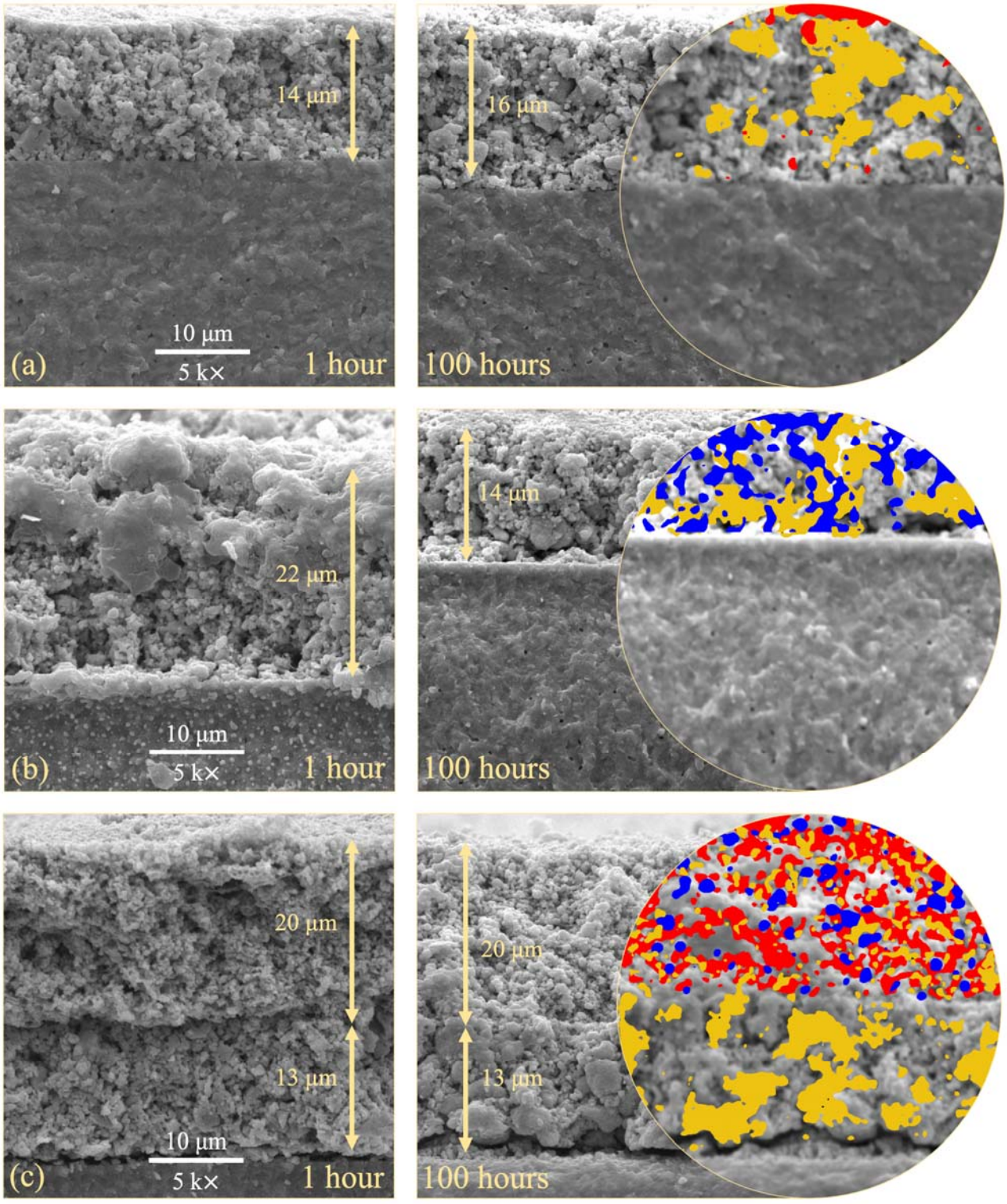

Figure 10: Scanning electron microscopy of the anode cross section. (a) Ceria-Co, (b) Ceria-Cu and (c) Ceria-Co-Cu anodes after 1h and 100h in hydrogen at 800˚C. The EDS detailed in circles shows phases distribution where Ceria is yellow, Cobalt is red and Copper is blue.

4.Conclusions

The bimetallic catalyst as well as its baseline monometallic compositions were successfully produced by the amorphous citrate method. H_2-TPR showed the ability of the metals to reduce and become catalytically active, as well as partial reduction of ceria that turned it into an oxygen-deficient ionic conductor structure. The presence of the oxygen-deficient ceria near the electrolyte interface is

supposed to aid ionic conductivity and increase oxygen ions supply to the three-phase boundaries, serving as buffer.

Cobalt-rich catalyst has shown its ability to operate as an SOFC nickel-free anode for the direct utilisation of carbonaceous fuels. Practical demonstrations in this work pointed out the necessity of operating constantly under load to avoid cracking that seemed to occur when no oxygen ions/electric current flow was present. The tests revealed that under OCV or OCV-simulated conditions, either the cells or the catalyst powder alone became prone to carbon deposition due to the lack of an oxidising agent. However, at least for the case of the bimetallic cell, when the cell was placed under load, eventual carbon deposits seemed to be oxidised by the oxygen ions, since there was no evidence of deposited carbon, neither in the Raman spectrum nor the TPO analysis.

The bimetallic cell was able to deliver from 350 to 550 $mW.cm^{-2}$, depending on the fuel stream, confirming that ceria with metallic loads is suitable for hydrocarbon electrooxidation without coking. Additionally, the comparison with the available literature for Ni-alloyed anodes as a benchmark, place the results within this work, as promising.

On the other hand, that was not the case for the cobalt monometallic cell. The absence of copper in this composition proved that the catalyst seemed to lose the ability to post-oxidise eventual carbon deposits, since its post-operation Raman spectrum showed massive presence of carbon. This confirmed the importance of copper, not only in enhancing electrical conductivity, but also for the adequate operation of the cells with hydrocarbons and alcohols. The bimetallic ensemble also demonstrates the ability of keeping a more homogeneous microstructure and phase distribution due to the inter-diffusion barrier formed between the different metallic species.

Acknowledgements

This work is supported by the Brazilian National Council of Technological and Scientific Development (CNPq) regarding a Split Fellowship PhD program, registered under the award number 200665/2015-4 and thus gratefully acknowledged by the authors.

References

[1] S. P. JIANG, Nanoscale and nanostructured electrodes of solid oxide fuel cells by infiltration: Advances and challenges., Int. J. Hydrogen Energy **37** 449 (2012).

[2] N. Mahato, A. Banerjee, A. Gupta, S. Omar, K. Balani, Progress in material selection for solid oxide fuel cell technology: A review., Prog. Mater. Sci **72** 141 (2015).

[3] N. Q. Minh, Ceramic fuel cells., J. Am. Ceram. Soc. **76** 563 (1993).

[4] P.E.V de Miranda, Science and Engineering of Hydrogen-Based Energy Technologies, 1st Edition, ELSEVIER, Academic Press (2019).

[5] J. Kihlman, J. Sucipto, N. Kaisalo, P. Simell, J. Lehtonen, Carbon formation in catalytic steam reforming of natural gas with SOFC anode off-gas., Int. J. Hydrogen. Energy **40** 1548 (2015).

[6] T. Chen, W. G. Wang, H. Miao, T. Li, C. Xu, Evaluation of car- bon deposition behavior on the nickel/yttrium-stabilized zirconia anode- supported fuel cell fueled with simulated syngas., J. Power Sources **196** 2461 (2011).

[7] S. Primdahl, B. F. Sørensen, M. Mogensen, Effect of Nickel Oxide/Yttria-Stabilized Zirconia Anode Precursor Sintering Temperature on the Properties of Solid Oxide Fuel Cells., J. Am. Ceram. Soc. **83** 489 (2004).

[8] J. R. Rostrup-Nielsen, J. B. Hansen, D. Helveg, N. Christiansen, A.-K. Jannasch, Sites for catalysis and electrochemistry in solid oxide fuel cell (SOFC) anode., Appl. Phys. A-Mater. **85** 427 (2006).

[9] B. Farrell, S. Linic, Direct electrochemical oxidation of ethanol on SOFCs: Improved carbon tolerance of Ni anode by alloying., Applied Catalysis B: Environmental **183** 386 (2016).

[10] I. Gavrielatos, D. Montinaro, A. Orfanidi, S. G. Neophytides, Thermogravimetric and Electrocatalytic Study of Carbon Deposition of Ag- doped Ni/YSZ Electrodes under Internal CH_4 Steam Reforming Conditions., Fuel Cells **9** 883 (2008).

[11] L. Troskialina, A. Dhir, R. Steinberger-Wilckens, Improved Performance and Durability of Anode Supported SOFC Operating on Biogas., ECS Trasactions **68** 2503 (2015).

[12] E. W. Park, H. Moon, M. soo Park, S. H. Hyun, Fabrication and characterization of Cu-Ni-YSZ SOFC anodes for direct use of methane via Cu-electroplating., International Journal of Hydrogen Energy **34** 5537 (2009).

[13] D. K. Niakolas, M. Athanasiou, V. Dracopoulos, I. Tsiaoussis, S. Be- belis, S. G. Neophytides, Study of the synergistic interaction between nickel, gold and molybdenum in novel modified NiO/GDC cermets, possible anode materials for CH_4 fueled SOFCs., Applied Catalysis A: General **456** 223 (2013).

[14] D. K. Niakolas, J. P. Ouweltjes, G. Rietveld, V. Dracopoulos, S. G. Neophytides, Au-doped Ni/GDC as a new anode for SOFCs operating under rich CH_4 internal steam reforming., International Journal of Hydrogen Energy **35** 7898 (2010).

[15] I. Gavrielatos, V. Drakopoulos, S. G. Neophytides, Carbon tolerant Ni-Au SOFC electrodes operating under internal steam reforming conditions., Journal of Catalysis **259** 75 (2008).

[16] C. A. Silva, P. E. V. Miranda, Synthesis of $LaAlO_3$ based materials for potential use as methane-fueled solid oxide fuel cell anodes., International Journal of Hydrogen Energy **40** 10002 (2015).

[17] W. Kiatkittipong, T. Tagawa, S. Goto, S. Assabumrun- grat, P. Praserthdam, Oxidative coupling of methane in the LSM/YSZ/LaAlO SOFC reactor., Journal of the Ceramic Society of Japan **37** 1461 (2004).

[18] T. Tagawa, K. K. Moe, T. Hiramatsu, S. Goto, Design of electrode for solid oxide fuel cells reactor., Solid State Ionics **106** 227 (1998).

[19] B. J. M. Sarruf, J.-E. Hong, R. Steinberger-Wilckens, P. E. V. de Miranda, CeO_2-Co_3O_4-CuO anode for direct utilisation of methane or ethanol in solid oxide fuel cells., Int. J. Hydrogen Energy **43** 6340 (2018).

[20] S. A. Venâncio, P. E. V. Miranda, Direct utilization of carbonaceous fuels in multifunctional SOFC anodes for the electrosynthesis of chemicals or the generation of electricity., Int. J. Hydrogen Energy **42** 13927 (2017).

[21] X.-F. Ye, S. R. Wang, Q. Hu, J. Y. Chen, T. L. Wen, Z. Y. Wen, Improvement of Cu-CeO_2 anodes for SOFCs running on ethanol fuels., Solid State Ion. **180** 276 (2009).

[22] L. Kundakovic, M. Flytzani-Stephanopoulos, Cu- and Ag-Modified Cerium Oxide Catalysts for Methane Oxidation., J. of Catalysis 179 **203** (1998).

[23] P. Wang, J. Zhang, Y. Bai, H. Xiao, S. Tian, H. Xie, G. Yang, N. Tsubaki, Y. Han, Y. Tan, Ternary copper-cobalt-cerium catalyst for the pro- duction of ethanol and higher alcohols through CO hydrogenation., App. Catalysis A **514** 14 (2016).

[24] W. L. Roth, The magnetic structure of CO_3O_4., J. Phys. Chem. Sol. **25** 1 (1964).

[25] I. B. Krynetskii, B. A. Gizhevskii, S. V. Naumov, E. A. Kozlov, Size Effect of the Thermal Expansion of Nanostructural Copper Oxide., Fizika Tverdogo Tela **50** 723 (2008).

[26] M. Chen, B. Hallstedt, A. N. Grundy, L. J. Gauckler, CeO_2-CoO Phase Diagram., J Am Ceram. Soc. **86** 1567 (2003).

[27] H. Okamoto, Cerium-Cobalt Binary Alloy Phase Diagram., ASM Alloy Phase Diagrams Center **2** 1047 (2007).

[28] W. Zhuang, Z. Y. Qiao, S. Wei, J. Shen, Thermodynamic evaluation of the Cu-R (R: Ce, Pr, Nd, Sm) binary systems., J. Phase Equilib. **17** 508 (1996).

[29] P. Knauth, G. Schwitzgebel, A. Tschöpe, S. Villain, Emf Measurements on Nanocrystalline Copper-Doped Ceria., J. Solid State Chem. **140** 295 (1998).

[30] J. Marrero-Jerez, A. Murugan, I. S. Metcalfe, P. Núñez, TPR-TPD-TPO studies on CGO/NiO and CGO/CuO ceramics obtained from freeze- dried precursors., Ceram. Int. **40** 15175 (2014).

[31] A. Pintar, J. Batista, S. Hocevarz, TPR, TPO, and TPD examinations of $Cu_{0.15}Ce_{0.85}O_{2-y}$ mixed oxides prepared by co-precipitation, by the sol-gel peroxide route, and by citric acid-assisted synthesis., J. Colloid Interface Sci. **285** 218 (2005).

[32] B. Wang, J. Zhu, Z. Lin, A theoretical framework for multiphysics modeling of methane fueled solid oxide fuel cell and analysis of low steam methane reforming kinetics., Appl. Energ. **176** 1 (2016).

[23] K. Ukai, Y. Mizutani, Y. Kume, O. Y. H. Yokokawa, S. C. Singhal, Solid Oxide Fuel Cells, vol. VII., Electrochemical Society, Pennington, NJ, (2001).

[34] J. Liu, S. A. Barnet, Operation of anode-supported solid oxide fuel cells on methane and natural gas., Solid State Ion. **158** 11 (2003).

[35] S.-I. Lee, K. Ahn, J. M. Vohs, R. J. Gorte, Cu-Co Bimetallic Anodes for Direct Utilization of Methane in SOFCs., Electrochem. Solid State Lett. **8** A48 (2005).

[46] S.-I. Lee, J. M. Vohs, R. J. Gorte, A Study of SOFC Anodes Based on Cu-Ni and Cu-Co Bimetallics in CeO_2YSZ., Journal of the Electrochemical Society **151** A1319 (2004).

[37] G. Balakrishnan, C. M. Raghavan, C. Ghosh, R. Divakar, E. Mohandas, J. I. Song, S. I. Bae, T. G. Kim, X-ray diffraction, Raman and photoluminescence studies of nanocrystalline cerium oxide thin films., Ceram. Int. **39** 8327 (2013).

[38] W. J. S. Schmid, R. Hausbrand, Cobalt oxide thin film low pressure metal-organic chemical vapor deposition., Thin Solid Films **567** 8 (2014).

[39] L. E. Gómez, J. F. Múnera, B. M. Sollier, E. E. Miró, A. V. Boix, Raman in situ characterization of the species present in Co/CeO_2 and Co/ZrO_2 catalysts during the COPrOx reaction., Int J Hydrogen Energy **41** 4993 (2016).

[40] A. Khana, C. Jiménez, O. Chaix-Pluchery, H. Roussel, J. L. Deschanvres, In-situ Raman spectroscopy and X-ray diffraction studies of the structural transformations leading to the $SrCu_2O_2$ phase from strontium-copper oxide thin films deposited by metalorganic chemical vapor deposition., Thin Solid Films **541** 136 (2013).

[41] F. C. Nix, F. E. Jaumot, Jr., Self-Diffusion in Cobalt, Phys. Rev. **82** 72 (1951).

[42] A. Kuper, H. Letaw, Jr., L. Slifkin, E. Sonder, C. T. Tomizuka, Self-Diffusion in Copper Phys. Rev. Phys. Rev. **98** 1870 (1955).

[43] K. M. Chow, W. Y. Ng, L.K. Yeung, Interdiffusion of Cu substrate/electrodeposits for Cu/Co, Cu/Co-W, Cu/Co/Ni and Cu/Co-W/Ni systems, Surface and Coatings Technology **99** 161 (1998).